



## Wearable breath monitoring via a hot-film/calorimetric airflow sensing system

Tao Jiang<sup>a,b,c,e</sup>, Lirong Deng<sup>d</sup>, Wenying Qiu<sup>a,b,c,e</sup>, Jiaming Liang<sup>a,b,c</sup>, Yichuan Wu<sup>f</sup>, Zhichun Shao<sup>b,c</sup>, Dongkai Wang<sup>a,b,c</sup>, Min Zhang<sup>e</sup>, Xiang Qian<sup>e,\*</sup>, Junwen Zhong<sup>b,c,g,\*</sup>, Xiaohao Wang<sup>a,e</sup>, Liwei Lin<sup>a,b,c,\*\*\*</sup>

<sup>a</sup> Sensors and Microsystems Laboratory, Tsinghua-Berkeley Shenzhen Institute, Tsinghua University, Shenzhen, 518055, China

<sup>b</sup> Berkeley Sensor & Actuator Center, University of California Berkeley, Berkeley, CA, 94720, USA

<sup>c</sup> Mechanical Engineering Department, University of California Berkeley, Berkeley, CA, 94720, USA

<sup>d</sup> Shenzhen Environmental Science and New Energy Technology Engineering Laboratory, Tsinghua-Berkeley Shenzhen Institute, Tsinghua University, Shenzhen, 518055, China

<sup>e</sup> Tsinghua-Shenzhen International Graduate School, Tsinghua University, Shenzhen, 518055, China

<sup>f</sup> School of Mechanical and Electrical Engineering, University of Electronic Science and Technology of China, Chengdu, 611731, China

<sup>g</sup> Department of Electromechanical Engineering, University of Macau, Macao, 999078, China

### ARTICLE INFO

#### Keywords:

Mobile health  
Breath monitoring  
Hot-film sensor  
Calorimetric sensor

### ABSTRACT

Monitoring the breath information from two nostrils can detect breath-related health problems. In this work, we introduce a wearable hot-film/calorimetric breath sensing system composed of a hot-film sensor in the center and two calorimetric sensors on two sides. This design has the advantages of low power consumption of 60 mW and good sensitivity to simultaneously measure the mix breath velocity and individual breath airflow signals from the two nostrils. In prototype demonstrations, abnormal breath conditions (apnea, hypopnea, polypnea) and the asymmetric breath conditions between the right and left nostril have been recorded and analyzed for potential usages in the diagnosis of specific breath-related diseases.

### 1. Introduction

Breath-related health problems, such as Apnea Syndrome, Asthma, and Obstructive Sleep Apnea Syndrome (OSAS), ... etc., are common diseases threatening human health (Jain et al., 2015; Vaessen et al., 2015; Meng et al., 2020; Su et al., 2020; Zhou et al., 2020). Specifically, OSAS is commonly found in 20–40% of elderly people and more than half of the patients are undiagnosed because of the requirement of the bulky and complex diagnostic equipment (Yaggi et al., 2005; Marin et al., 2005). One standard and precise way to diagnose OSAS is based on the polysomnography (PSG), which means the patients or volunteers should wear cumbersome devices during sleeping (Ghassemi et al., 2018). In addition, viral pneumonia has become a vital threaten to human life worldwide, and breath monitoring is meaningful to the clinical confirmation of pneumonia when facing unknown virus-related pneumonia (Korppi et al., 2008; Watkins and Lemonovich, 2011). One

of the important and effective methods for diagnosing the breath-related disease is to measure and analyze the breath airflow conditions continuously from the nostrils. Generally, there are two schemes for breath airflow measurement defined as indirect measurement scheme and direct measurement scheme (Table S1) (Massaroni et al., 2019b; Massaroni et al., 2019a; Schon et al., 2018; Ciaffoni et al., 2016; Dominelli and Sheel, 2012; Shao et al., 2014; Schena et al., 2015; Goreke et al., 2015; Yahya and Faezipour, 2014; Nam et al., 2016; Avalur, 2013; Yoon et al., 2014; Bates et al., 2010; Chan et al., 2013; Lapi et al., 2014; Lewis et al., 2011; Basu et al., 2016; Pereira et al., 2015; Seppä et al., 2010; Frasca et al., 2015; Bifulco et al., 2014; Mahbub et al., 2017; Liu et al., 2017; Cao et al., 2012; Dinh et al., 2017). There are several approaches for the indirect measurement scheme, including fiber-optic sensors (Schena et al., 2015), 3D image sensors (Stehning et al., 2005), and ultrasonic sensors (Arlotto et al., 2014) to detect variations of chest movements. However, this indirect measurement scheme is easily

\* Corresponding author. Department of Electromechanical Engineering, University of Macau, Macao, 999078, China.

\*\* Corresponding author. Tsinghua-Shenzhen International Graduate School, Tsinghua University, Shenzhen, 518055, China.

\*\*\* Corresponding author. Sensors and Microsystems Laboratory, Tsinghua-Berkeley Shenzhen Institute, Tsinghua University, Shenzhen, 518055, China.

E-mail addresses: [qian.xiang@sz.tsinghua.edu.cn](mailto:qian.xiang@sz.tsinghua.edu.cn) (X. Qian), [junwenzhong@um.edu.mo](mailto:junwenzhong@um.edu.mo) (J. Zhong), [lwlin@berkeley.edu](mailto:lwlin@berkeley.edu) (L. Lin).

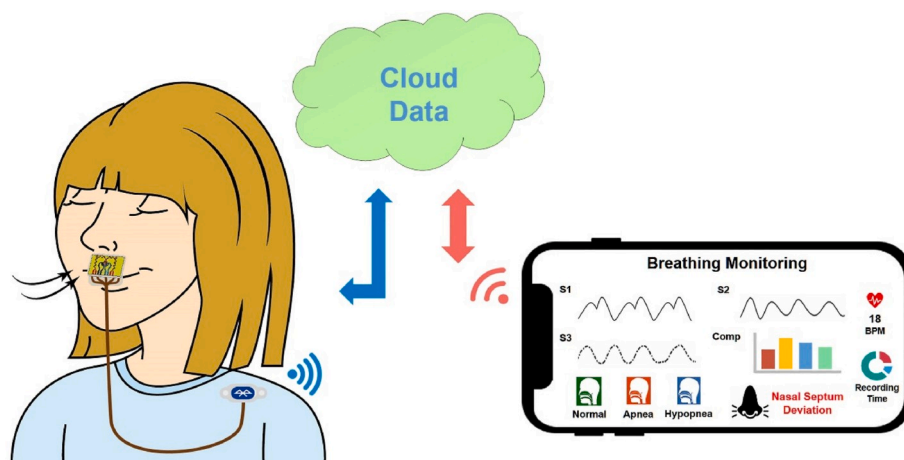


**Fig. 1.** Conceptual drawing for a mobile health system based on the wearable hot-film/calorimetric breath sensing system with three channels to measure the normal or abnormal breath data, which will be sent to the Cloud to be processed and analyzed.

affected by random body movements to result in invalid results (Bates et al., 2010; Shao et al., 2014). Furthermore, this method can't measure the individual airflow signals from the two nostrils, which is critical for the diagnosis of common breath-related diseases, such as Nasal Polyp and Nasal Septum. The approaches of direct measurement scheme includes pressure-based flow sensors such as piezoelectric sensors (Bifulco et al., 2014; Liu et al., 2017; Mahbub et al., 2017; Yoon et al., 2014) and piezoresistive sensors (Chu et al., 2019; Jeong et al., 2009), thermal-based flow sensors (hot-film sensors (Mailly et al., 2001), time-of-flight sensors (Meng et al., 2008), and calorimetric sensors (Dinh et al., 2017)). Combining with wearable electronics (Chen et al., 2016; Su et al., 2016; Yan et al., 2020; Zhang et al., 2020), these systems are useful for portable and wearable breath monitoring tools with the potential to be integrated as sensor arrays for breath airflow measurements. Specifically, thermal-based flow sensors have small size, simple structure, and are easy for integration (Scheda et al., 2015; Zhao and Zhu, 2017). Hot-film sensors based on a self-heated fine wire has high sensitivity but the heating requirement can cause high power consumption. Calorimetric sensor is heated up by ambient heat source and has low power consumption but the sensitivity and stability need to be further improved (Montuschi et al., 2013). Thus, the integration of hot-film sensor and calorimetric sensor as a sensing system could be a good method to take advantages from both schemes.

Herein, we propose a wearable hot-film/calorimetric sensing system for real-time breath monitoring, in which the system is composed of a hot-film sensor (Heater/Sensor-1) in the center and two calorimetric sensors (Sensor-2 and Sensor-3) at two sides. The power consumption for the system is about 60 mW and the system can simultaneously measure the mix airflow velocity from the two nostrils with Heater/Sensor-1 and individual breath airflow signals from right and left nostril independently with Sensor-2 and Sensor-3. Two important demonstrations are achieved: (1) abnormal breath conditions such as apnea, hypopnea, and polypnea clearly recognized by Heater/Sensor-1; (2) asymmetric breath conditions for right and left nostrils by Sensor-2 and Sensor-3 characterized by the Dynamic Time Warping (DTW) algorithm. As indicated in the concept illustration in Fig. 1, the normal and abnormal breath data measured by the three-channel wearable system could be processed and analyzed by sending the data to the Cloud wirelessly and then showed the results in the portable electronics.

## 2. Experimental section

### 2.1. Fabrication of the wearable hot-film/calorimetric breath sensing system

The fabrication begins with a 2-inch Si wafer coated with a 500 nm-thick poly(methyl methacrylate), followed by coating 5  $\mu$ m-thick polyimide (Figs. S1-I). The photolithography process is done after a Cr (6 nm)/Au (100 nm) deposition by the electron beam evaporation process to define the locations of Sensor/Heater-1, Sensor-2, Sensor-3, interconnections, and bonding pads for external electrical connections (Fig. S1-II). The second layer of polyimide (thickness of 5  $\mu$ m) is deposited on top of the Heater/Sensor-1, Sensor-2, and Sensor-3 (Fig. S1-III) to provide electrical insulation and possible isolation from mechanical strain. Reactive ion etching of the polyimide defines the mesh layout of the array and exposes the bonding pads. Thin conductive cables are bonded at the periphery via the hot-pressing method as the interconnections to external electronics. Afterwards, a waterproof dressing tape (3M) is used to enable the removal of the structure from the Si wafer by immersing the system into a warm water bath (Fig. S1-IV). The frame of the medical tape (3M) is used to provide mechanical support for the system (Fig. S2).

### 2.2. Temperature coefficient of resistance calibration

The temperature coefficient of resistance is calibrated using a hot-plate (IKA C-MAG HS 7 S001) and a digital multi-meter (Innova 3320) (Fig. S3) under the room temperature of 25  $^{\circ}$ C. The detailed calibration results for Heater/Sensor-1, Sensor-2, and Sensor-3 are shown in Fig. S4.

### 2.3. Airflow velocity calibration

As indicated in Fig. S5, the flow source is supplied by a nitrogen cylinder and controlled by the flow valve. The airflow velocity is measured by the flow meter (Xima AR866A). The Heater/Sensor-1 is heated by a constant current of 4 mA provided by a precision current source (Keithley 6222) and the output signals under various airflow velocity are measured by an electrometer (Keithley 6514) and a data acquisition card (NI USB-6314). In this case, the 4-wire method is used to power and measure the Heater/Sensor-1. The output signals of Sensor-2 and Sensor-3 are measured by a multichannel resistance meter (Keysight data acquisition switch unit 34970A). In order to provide the RH 100% environment, an ultrasonic cooling mist humidifier (Intertek PEHUMIDIF) is used.

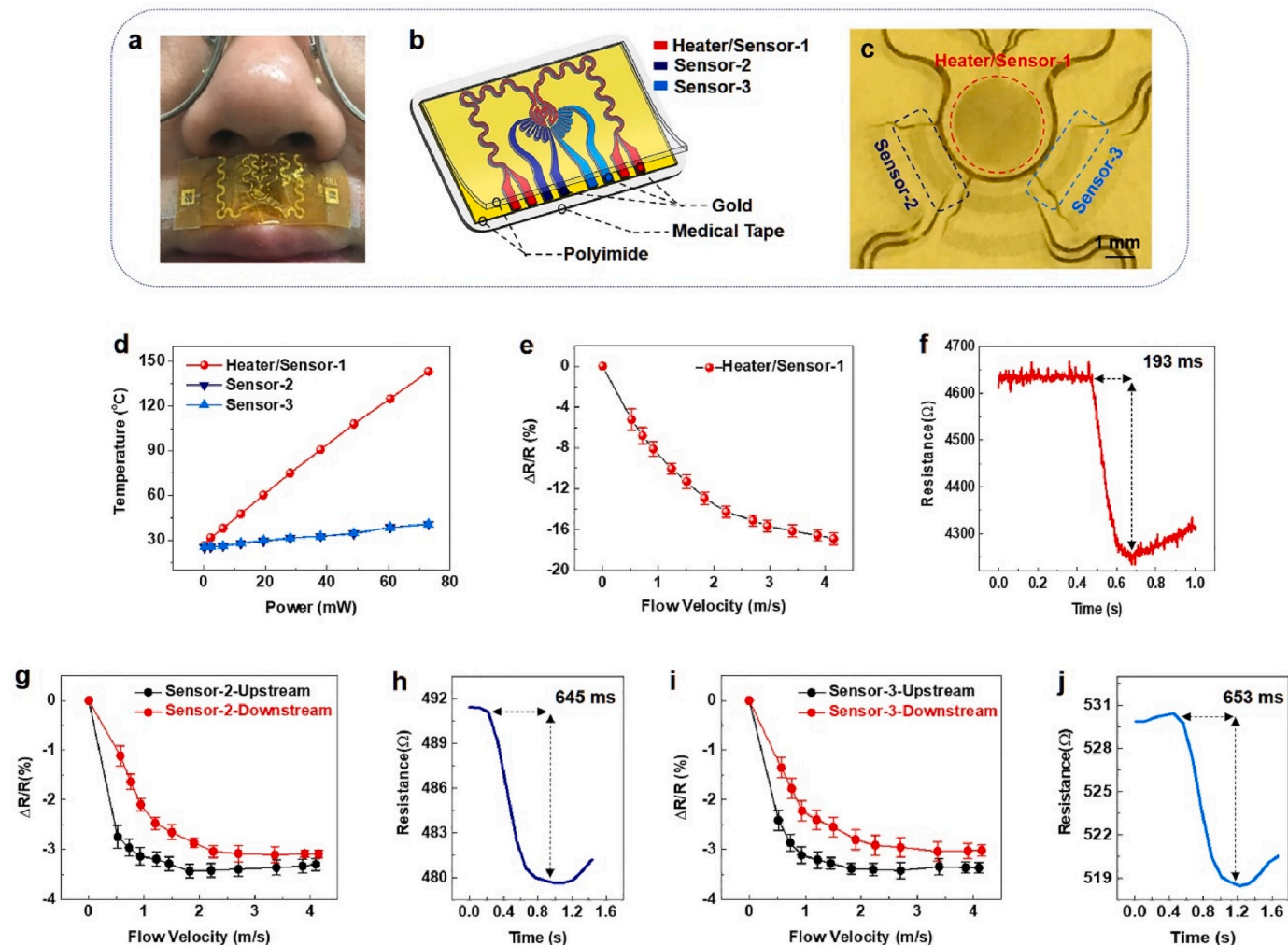


**Fig. 2.** Design and working mechanism of the wearable hot-film/calorimetric breath sensing system. (a) Image depicting a prototype breath sensing system below the nose to detect human breath conditions. (b) Schematic diagram showing the structure and material of the breath sensing system. The whole device is composed of two PI films to encapsulate the gold patterns and a medical tape is used to attach the device to human skin. Sensor-2 and Sensor-3 locate at two sides of the Heater/Sensor-1 (Hot-Film type), which is the only device to be heated up by the external power. (c) Enlarged image showing the locations of Heater/Sensor-1, Sensor-2, and Sensor-3 on a prototype device. (d) Temperatures measurement results on Heater/Sensor-1, Sensor-2, and Sensor-3 under various working power of Heater/Sensor-1 from 0 to 75 mW. (e) The calibration results of Heater/Sensor-1 for the relative resistance change with respect to airflow velocity from 0 to 4 m/s, under a working power of 60 mW. (f) The measured response time for Heater/Sensor-1 when the working power is 60 mW under an airflow velocity of 1 m/s. (g) Sensor-2 and (i) Sensor-3 calibrations results of relative resistance change with respect to airflow velocity for upstream (inhaling) and downstream (exhaling) conditions. The response time for (h) Sensor-2 and (j) Sensor-3 for the prototype tests under the airflow velocity of 1 m/s and a working power of 60 mW. (For interpretation of the references to colour in this figure legend, the reader is referred to the Web version of this article.)

### 3. Results and discussion

#### 3.1. Design and working mechanism

The fabricated wearable hot-film/calorimetric breath sensors array is attached on the upper lip of a volunteer to monitor the breath conditions, as depicted in Fig. 2a. The structure of the breath sensing system has two PI films to encapsulate the three sensors made of gold patterns, as in Fig. 2b, including Heater/Sensor-1, Sensor-2, and Sensor-3, respectively. By designing the size and shape of the sensing parts and interconnection, the measured resistance variation is mainly from the sensing parts. Heater/Sensor-1 locates at the center and the operation mechanism is the Hot-Film type airflow sensor. Sensor-2 and Sensor-3 are at the two sides of Heater/Sensor-1 and they are the Calorimetric type airflow sensor. Only Heater/Sensor-1 is powered and heated up. Fig. 2c shows the image of a prototype breath sensing system, where Heater/Sensor-1 has the circular-shape and Sensor-2/3 have the arc-

shape, while all three sensors have the sizes of several millimeters.

Under various working power levels (0–75 mW) on Heater/Sensor-1, the temperature values of the three sensors increase linearly as the working power increases as recorded in Fig. 2d. When the power reaches 60 mW, the temperature of Heater/Sensor-1 is 125 °C and the temperatures of Sensor-2 or Sensor 3 are about 38.4 °C. This temperature is higher than the human body temperature, which is critical to assure both Sensor-2 and Sensor 3 can avoid the interferences from the human body heat. In general, a high temperature condition is helpful to increase the outputs and stability for these sensors (Fig. S6).

Under a working power of 60 mW, the relative resistance changes ( $\Delta R/R$ ) with respect to the airflow velocity of Heater/Sensor-1 are calibrated. The maximum velocity is set to be about 4 m/s (close to the maximum breath velocity) and the  $\Delta R/R$  value is about 16.7%, as shown in Fig. 2e. Moreover, the response time for Heater/Sensor-1 under a typical airflow of 1 m/s is about 193 ms, as indicated in Fig. 2f. The calibrations for Sensor-2 and Sensor-3 under upstream

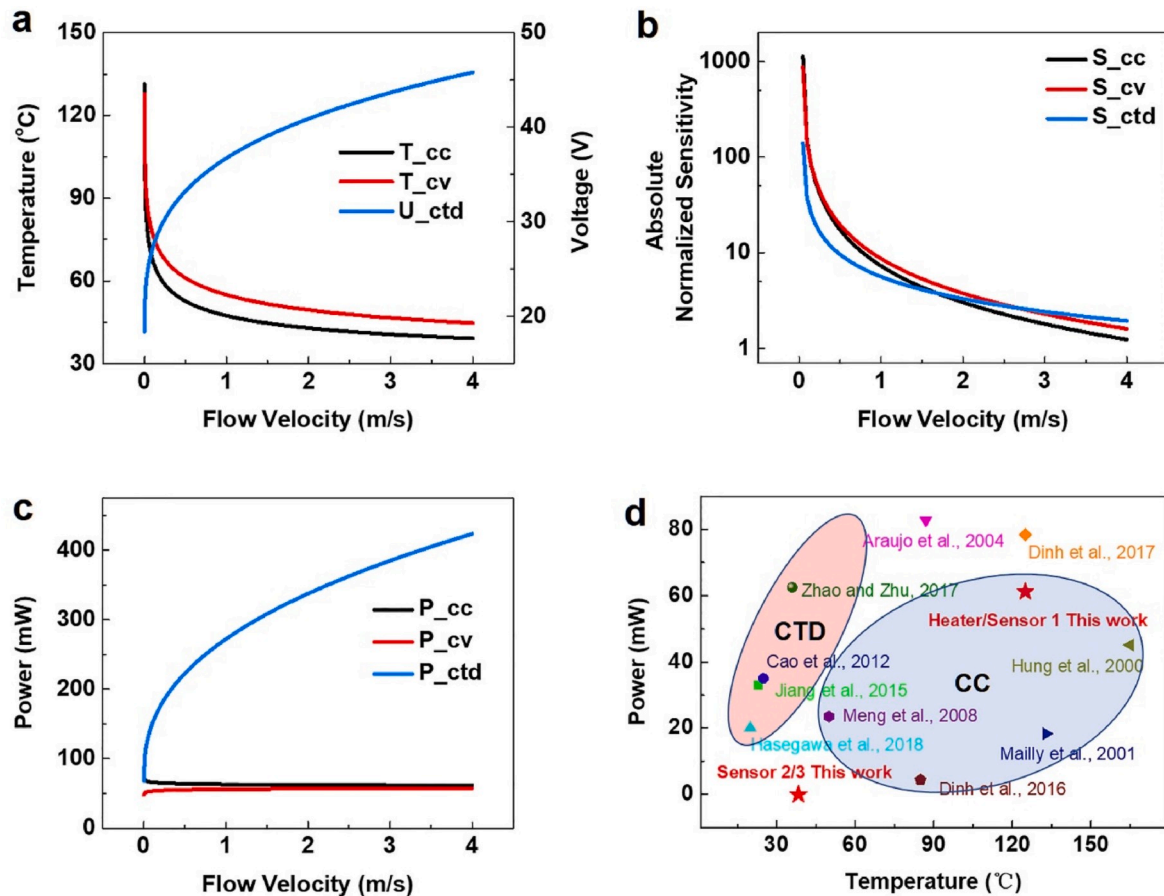


**Fig. 3.** Matlab simulation results of the working temperature and working power for the wearable hot-film/calorimetric breath sensing system under three heating modes: Constant Current (CC), Constant Voltage (CV) and Constant Temperature Difference (CTD). (a) Working temperature on Heater/Sensor-1 under the three heating modes, with the air flow velocity from 0 to 4 m/s. (b) Absolute normalized slope of the three curves in (a) to depict the output sensitivity of the three heating modes. (c) Working power for Heater/Sensor-1 under the three heating modes. (d) Comparison of working temperature and working power between the prototype breath sensing system and previous reported, thermal-based sensors.

(emulating the inhaling process) and downstream conditions (emulating the exhaling process) are conducted as shown in Fig. 2g and i, and the absolute  $\Delta R/R$  values show the upstream condition will results in a bit larger values than those of the downstream condition. In the upstream condition, Sensor-2 and 3 are cooled more due to the less heat from the Heater/Sensor-1, thus to induce a larger temperature change than that of the downstream condition. Experimentally, under the airflow velocity of 4 m/s, the absolute  $\Delta R/R$  values for upstream and downstream conditions are about 3.5% and 3%, respectively. On the other hand, the response times for Sensor-2 and Sensor-3 are 645 ms and 653 ms under the air flow speed of 1 m/s, respectively, as shown in Fig. 2h and j. Such response time is good enough for breath measurements, as the breath periods for all conditions (including polypnea condition) are normally lower than 100 bpm. It should be noted that the performances such as  $\Delta R/R$  values and response times of Sensor-2 and Sensor-3 are not as good as those of Heater/Sensor-1, as the working temperature of Heater/Sensor-1 (125 °C) is higher. All three sensors show excellent stability even under a working environment with relative humidity of 100% for 60 min (Fig. S7), implying this sensing system is suitable to measure breath conditions in various environments.

### 3.2. Optimization of heating mode

Three control modes are applied for heating controls, which are constant current (CC), constant voltage (CV), and constant temperature difference (CTD) modes (Al-Khalidi et al., 2011; Que and Zhu, 2012; Ciaffoni et al., 2016). For CC and CV mode, the output is temperature

while for the CTD mode, the output is voltage. The 4-wire method is utilized in the setup for Heater/Sensor-1 by providing a constant current and recording the change of voltage. Under this situation, the resistance ( $R_w$ ) of Heater/Sensor-1 at a specific working temperature can be calculated (Dinh et al., 2017):

$$R_w = U_h / I_c \quad (1)$$

Where  $I_c$  is the constant current and  $U_h$  is the measured output voltage. The working temperature change ( $\Delta T$ ) as compared to room temperature (25 °C) of Heater/Sensor-1 can be calculated (Que and Zhu, 2012):

$$\Delta T = (R_w / R_{25} - 1) / \alpha_h \quad (2)$$

Where  $R_{25}$  is the resistance value of the sensors at 25 °C;  $\alpha_h$  is the temperature coefficient of resistance (Fig. S4). The working temperature ( $T_w$ ) of Heater/Sensor-1 can be obtained as:

$$T_w = 25 + \Delta T \quad (3)$$

This formula is the theoretical basis for solving the problem of heat dissipation to determine the conversion between the flow rate and heat dissipation rate. It describes the heat dissipation as (Bruun, 1996; Schena et al., 2015):

$$H_{inf} = a + b \cdot v^{0.5} \quad (4)$$

Where  $H_{inf}$  is the total heat dissipation rate of the long hot wire;  $v$  is the free flow velocity of the medium; and its direction is perpendicular to the hot film. Constant coefficients  $a$  and  $b$  are parameters related to



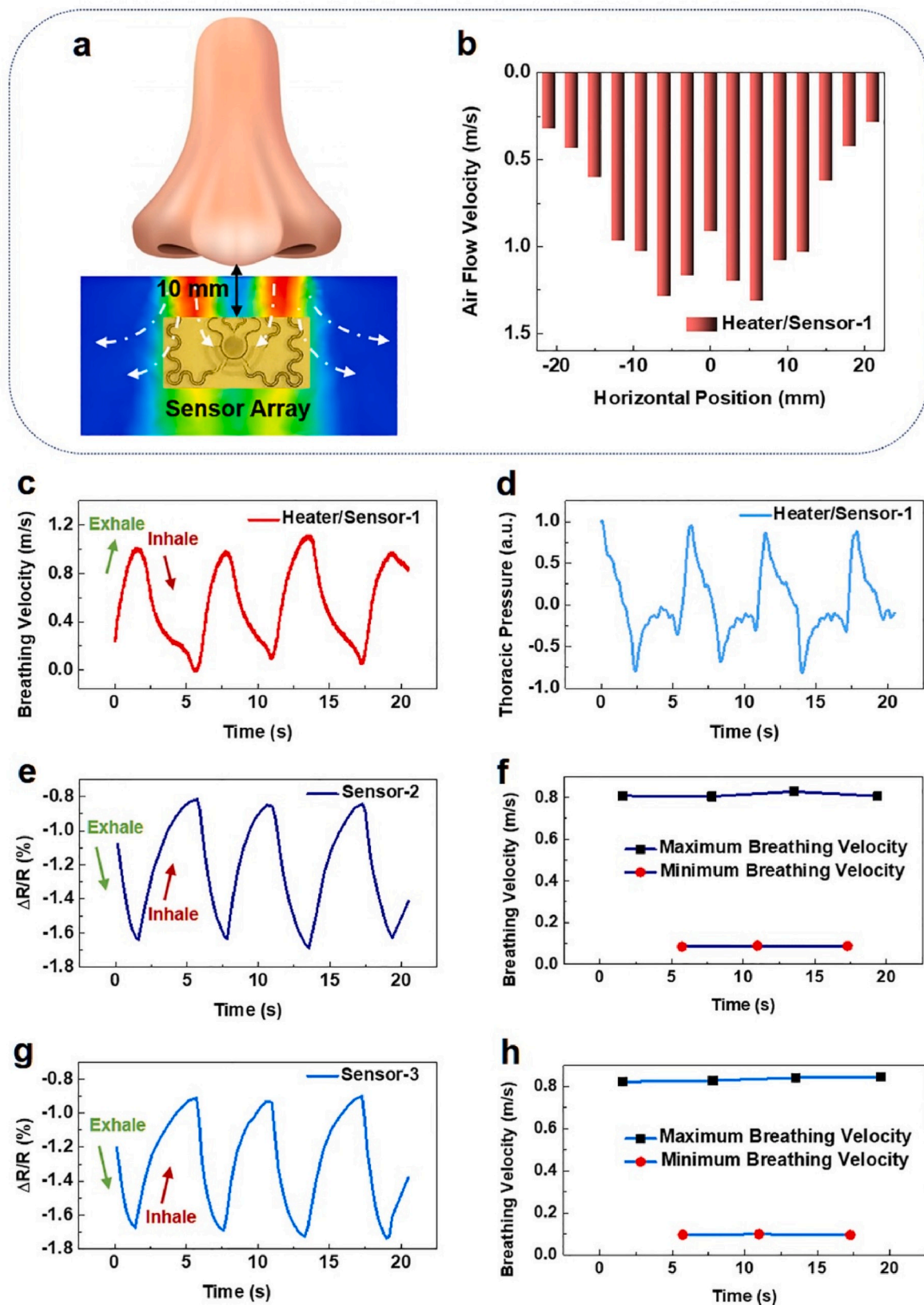


**Fig. 4.** Measurement results for the prototype wearable hot-film/calorimetric breath sensing system under normal breath conditions. (a) Schematic diagram depicting the airflow distribution under the normal breath condition by placing the device 10 mm under the two nostrils. (b) The airflow velocity measured by Heater/Sensor-1 by placing the system at different horizontal positions, with the center of two nostrils as the origin. (c) The breath velocity vs. time; and (d) the corresponding relative thoracic pressure vs. time measured by using Heater/Sensor-1 during the continuous exhaling and inhaling process. (e) The resistance vs. time; and (f) corresponding maximum/minimum breath velocity measured by Sensor-2. (g) The resistance vs. time; and (h) corresponding maximum/minimum breath velocity measured by Sensor-3.

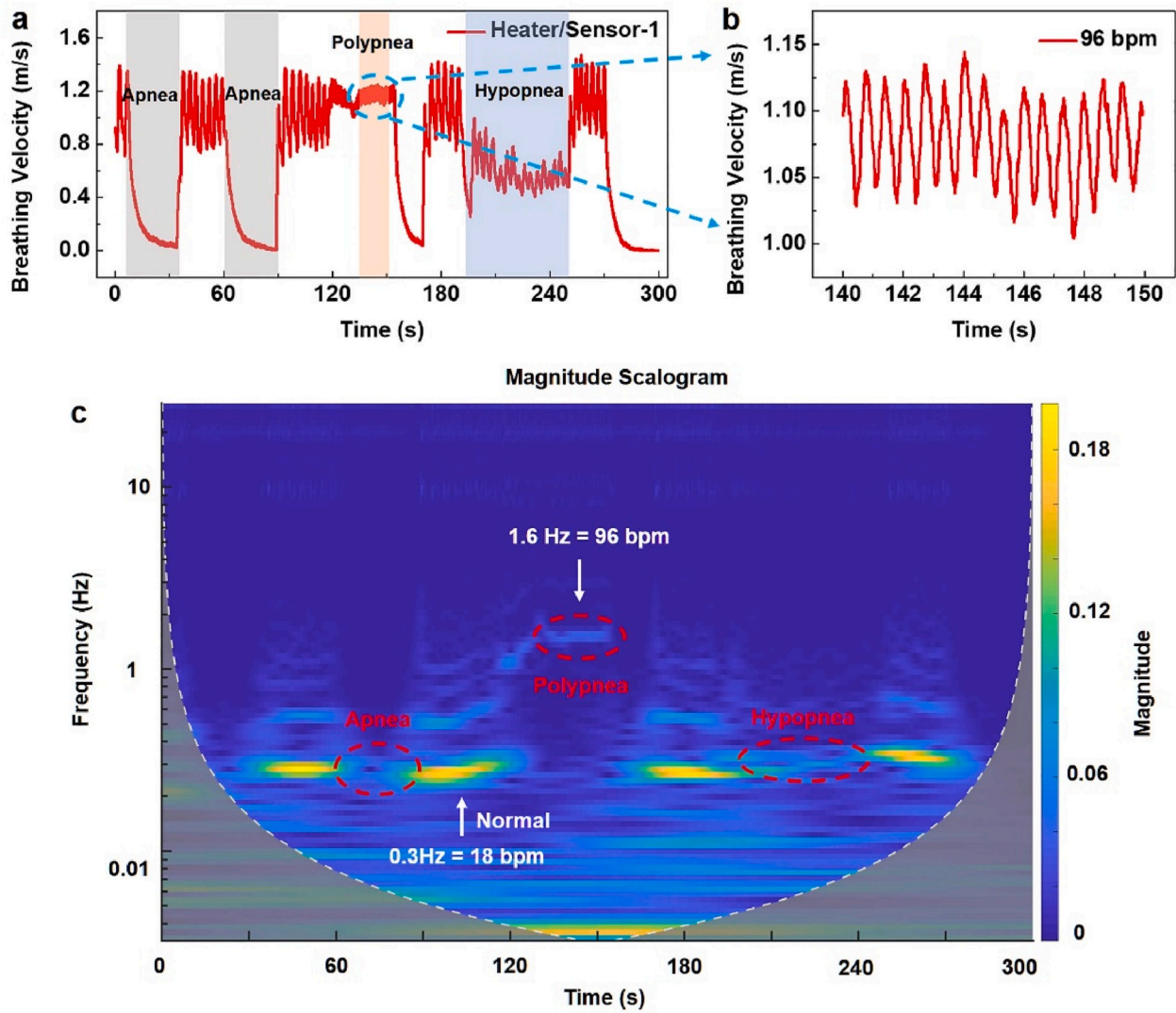


**Fig. 5.** Abnormal breath conditions measurement results detected by the prototype system. (a) The breath velocity vs. time measured by Heater/Sensor-1 for apnea, hypopnea, and polypnea. (b) The specific breath velocity vs. time results for polypnea. (c) The Continuous Wavelet Transforming results for breath velocity vs. time results in (a) to show the frequency and magnitude parameters of apnea, hypopnea, and polypnea.

the thermal conductivity, density, molecular viscosity, Prandtl number and the diameter of the hot film. The working power of the Heater/Sensor-1 ( $P$ ) can be calculated as (Bruun, 1996):

$$P = H_{inf} \cdot \Delta T \quad (5)$$

The working power of Heater/Sensor-1 and the working temperature of three sensors are calculated with Matlab Software with aforementioned equations. In the CC and CV modes, the working temperature decreases when the airflow velocity increasing. The CTD mode works under constant temperature (20–70 °C) and is characterized by output voltage. As shown in Fig. 3a, the CC mode has lower working temperature than that of the CV mode with airflow velocity from 0 to 4 m/s. In order to evaluate the performances of the three modes, we calculate the absolute normalized sensitivity. The sensitivity of CC mode is almost the same as those of the other two modes, as indicated in Fig. 3b. Moreover, the working power of Heater/Sensor-1 is almost the same as those for CC and CV modes, while the CTD mode has much higher power consumption (Fig. 3c), due to the CTD mode needs keeping constant high temperature. According to the above results, CC mode is chosen as the heating mode in this work for low power consumption, reasonable sensitivity, and relatively high temperature operations. The comparison of working temperature and working power between our breath sensing

system and previous reported thermal-based sensors are depicted in Fig. 3d (Araujo et al., 2004; Cao et al., 2012; Dinh et al., 2017, 2016; Hasegawa et al., 2018; Hung et al., 2000; Jiang et al., 2015; Mailly et al., 2001; Meng et al., 2008; Zhao and Zhu, 2017). It can be seen that the working temperature of Heater/Sensor-1 is reasonably high and the total working power is about 60 mW, while Sensor-2 and 3 don't require any power consumption.

### 3.3. Normal breath conditions

In practical measurements, the placement of the sensing system is important. During the preliminary tests, the system is placed about 10 mm under the two nostrils and its horizontal location could significantly affect the measurement results. The airflow distribution under the normal breath condition is simulated and depicted in Fig. 4a. For the vertical position, by placing the sensors array with 10 mm away from the center of the two nostrils is reasonable. In such vertical position, the mixed air flow from the two nostrils is strong enough. For the horizontal position, the maximum airflow speed measured by Heater/Sensor-1 with respect to the horizontal positions (by defining the center of the two nostrils as the origin) is shown in Fig. 4b and Fig. S8. The velocity distributions are functioned to calibrated the central position. As

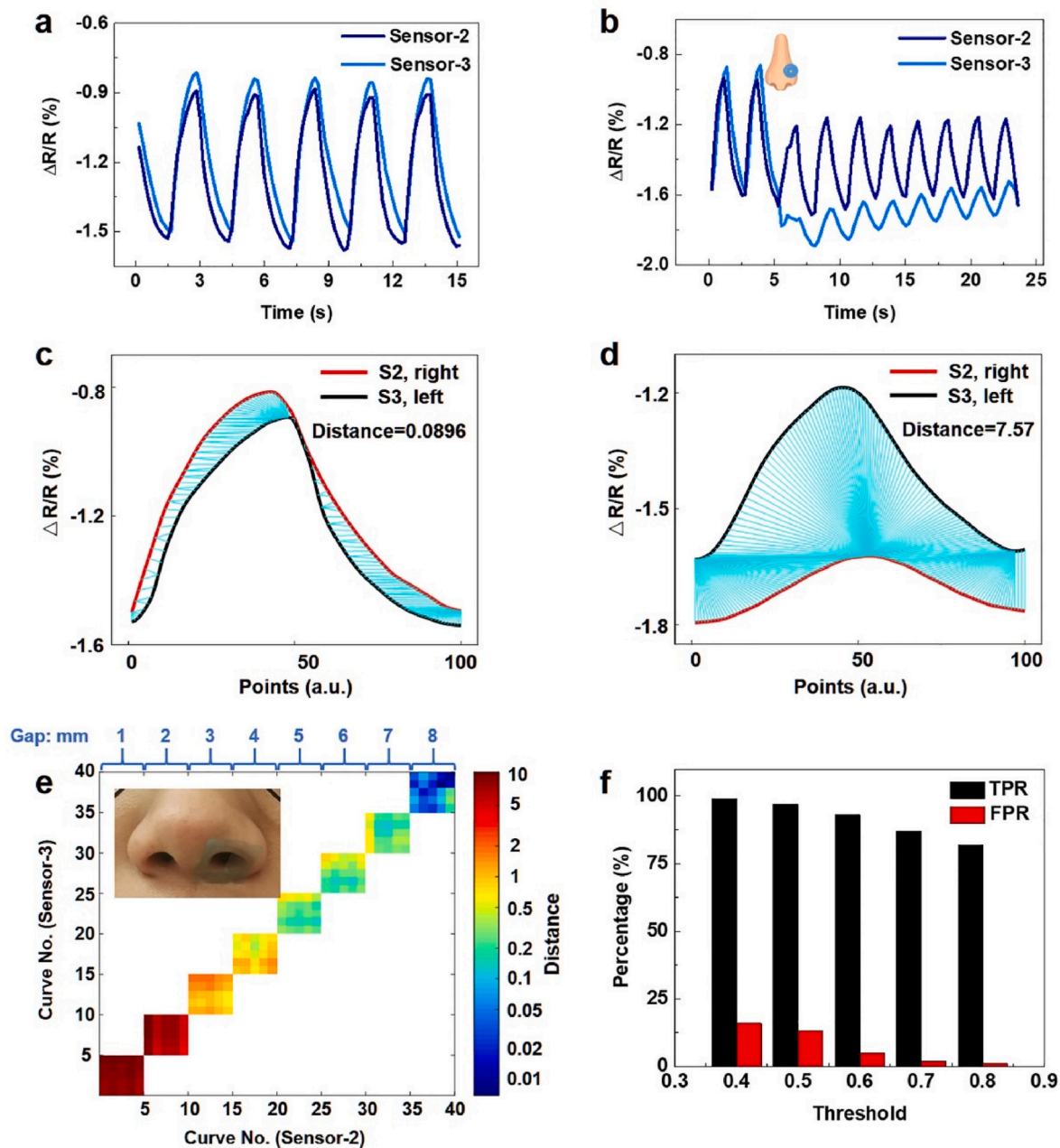


**Fig. 6.** Breath symmetry evaluations for the two nostrils. (a) The resistance changes vs. time plots for Sensor-2 (right nostril) and Sensor-3 (left nostril) under the normal breath condition. (b) The resistance changes vs. time plots for Sensor-2 and Sensor-3 when the left nostril is mechanically pressed. The distance between the curves measured by Sensor-2 and Sensor-3 with the DTW algorithm for (c) normal breath condition; and (d) the left nostril is mechanically pressed. Small distance value implies good similarity of the results measured by Sensor-2 and Sensor-3. (e) Calculated DTW distance matrix between the results measured by Sensor-2 and Sensor-3, where the gap for left nostril varies from 1 to 8 mm controlled by a square-shape mask as shown in the inset. (f) Setting the different distance values as the thresholds to characterize the asymmetric breath based on the true positive (TPR) rate and false positive rate (FPR) values.

expected, the results are symmetric to the origin (center) of the horizontal location and the system should be  $-6$  to  $6$  mm around the center of the two nostrils, so that to make Heater/Sensor-1 measure the strong and stable mixed airflow from two nostrils, simultaneously, Sensor-2 and Sensor-3 mainly record airflows from the individual left and right nostril, respectively.

The breath velocity vs. time curves measured by Heater/Sensor-1 under the normal breath condition is shown in Fig. 4c. The maximum breath velocity for a 30 years old male volunteer is about  $0.9$ – $1.1$  m/s and the exhaling and inhaling processes are unsymmetrical to each other. By integrating the breath velocity curves, the pulmonary pressure curves are obtained, as depicted in Fig. 4d. The pressure variation

explains the unsymmetrical breath velocity is caused by the slower and gentler pressure change during the inhaling process. Sensor-2 and Sensor-3 measure the breath signals from the single nostril of this volunteer and also show the asymmetric effect for exhaling and inhaling processes (Fig. 4e and g). Moreover, the maximal and minimum breath velocity for right and left nostril is close, which are about  $0.9$  m/s and  $0.1$  m/s, respectively, as depicted in Fig. 4f and h.

#### 3.4. Abnormal breath conditions

Some dangerous diseases, such as stroke, OSAS, and cardiovascular disease, may accompany abnormal breath conditions like apnea,



hypopnea, and polypnea. In this work, abnormal breath conditions are factiously created by a 30 years old male volunteer and the corresponding breath velocity vs. time curves are continuously measured by Heater/Sensor-1, as depicted in Fig. 5a. It is found that apnea will show suddenly decreased breath velocity and hypopnea will show obvious lower breath velocity and disordered breath patterns. If polypnea occurs, the breath period will largely increase and as shown in Fig. 5b, the breath period increases from about 18 bpm for normal condition to 96 bpm. Continuous Wavelet Transform (CWT) results for the breath velocity vs. time plots are provided to show the frequency and magnitude of abnormal breath conditions, as depicted in Fig. 5c. Each abnormal breath condition has its own specific frequency and magnitude pattern and can be differentiated. Specifically, apnea has the patterns with the interruptions of frequency and magnitude parameters; hypopnea has the pattern of low magnitude parameter; and polypnea has the pattern of high frequency signals. As such, these frequency and magnitude analysis of breath signals by the CWT method have the potential to be used to diagnose breath-related diseases.

### 3.5. Breath symmetry evaluations from two nostrils

Asymmetric breath conditions from two nostrils often occurs when people catch a cold or have nasal polyp disease. Sensor-2 and Sensor-3 on the breath sensing system can measure the airflow from right and left nostril independently to evaluate the asymmetric breath conditions. Fig. 6a shows the measured signal intensity from Sensor-2 and Sensor-3 are similar under the normal breath condition. By mechanically pressing the left nostril, which makes the flow tube become narrower, the measured signal intensity ( $\Delta R/R$  value) of Sensor-3 increases drastically, while the intensity of Sensor-2 also increases a bit, as shown in Fig. 6b. In time series analysis, Dynamic Time Warping (DTW) algorithm (Churi et al., 2017; Petitjean et al., 2011; Myers and Rabiner (1981); Senin (2008)) is one of the algorithms for measuring similarity between two temporal sequences. Herein, the DTW algorithm is applied to analyze the measured signals from two nostrils. Specifically, the time series curves are truncated into a single period and resampled to 100 points for each cycle, and the distance values between two typical cycles are obtained as shown in Fig. S9. A large distance means low similarity of the signals, which implies the asymmetric breath condition. For normal breath condition, the distance between two typical cycles from the Sensor-2 and Sensor-3 is small at 0.0896 (Fig. 6c). After mechanically pressing the left nostril, the distance increases to 7.57 (Fig. 6d), significantly showing the asymmetric breath condition. In order to systematically characterize the asymmetric breath condition, square shape masks are placed on the left nasal to control the air flow (inset in Fig. 6e) to form variable effective gap for breath airflow from 1 to 8 mm. For each gap condition, five cycles of measurements are randomly selected from the 2-min data collected from Sensor-2 and Sensor-3. The calculated DTW distance matrix in Fig. 6e shows that smaller effective gap will results in higher asymmetric breath condition as expected. When the effective gap is 1 mm, the distance values reach to around 10. Calculated distance values are below 0.05 for effective gap of 8 mm (close to normal breath condition). By setting the threshold based on distance using the DTW distance matrix, the identification process for the asymmetric breath condition can be characterized (where TPR is the true positive rate and FPR is the false positive rate) based on the threshold values as shown in Fig. 6f and Fig. S10. Setting the threshold at large distance means critical judgement for the happening of asymmetric breath conditions.

## 4. Conclusion

In summary, a wearable hot-film/calorimetric breath sensing system composed of a Heater/Sensor-1 (hot-film type) at the center position and Sensor-2/Sensor-3 located on two sides (calorimetric type) has been designed, fabricated and tested to measure the breath airflow

information. Heater/Sensor-1 acts as the functional unit to measure the mix airflow velocity from the two nostrils, and it be heated up by external electrical power. Sensor-2 and Sensor-3 are not self-heated but be heated by being close to the Heater/Sensor-1 to measure the individual breath airflow signals from each nostril. Experimental results show that Heater/Sensor-1 can clearly recognize the abnormal breath conditions, such as apnea, hypopnea, and polypnea by analyzing the frequency and magnitude patterns from the breath velocity signals. On the other hand, processed by the DTW algorithm, signals from Sensor-2 and Sensor-3 can be used to characterize the asymmetric breath condition between right and left nostril, which is critical for diagnosing common breath-related diseases, such as Nasal Polyp and Nasal Septum.

## Declaration of competing interest

The authors declare that they have no known competing financial interests or personal relationships that could have appeared to influence the work reported in this paper.

## CRediT authorship contribution statement

**Tao Jiang:** Writing - original draft, Investigation. **Lirong Deng:** Validation, Formal analysis. **Wenyong Qiu:** Validation. **Jiaming Liang:** Validation. **Yichuan Wu:** Visualization. **Zhichun Shao:** Visualization. **Dongkai Wang:** Visualization. **Min Zhang:** Supervision. **Xiang Qian:** Supervision, Validation, Writing - review & editing. **Junwen Zhong:** Investigation, Writing - review & editing, Supervision. **Xiaohao Wang:** Supervision. **Liwei Lin:** Writing - review & editing, Supervision.

## Acknowledgements

This work was supported in part by the National High Technology Research and Development Plan of China (2015AA043505) and in part by Shenzhen Fundamental Research Funding (Grant No. JSGG20180508153002284). Prof. X.W. and Prof. L.L. are core-principal investigators of Tsinghua-Berkeley Shenzhen Institute (TBSI) and we acknowledge the funding support of TBSI.

## Appendix A. Supplementary data

Supplementary data to this article can be found online at <https://doi.org/10.1016/j.bios.2020.112288>.

## References

- Al-Khalidi, F.Q., Saatchi, R., Burke, D., Elphick, H., Tan, S., 2011. *Pediatr. Pulmonol.* 46, 523–529.
- Araujo, G.A.L., Freire, R.C.S., Silva, J.F., Oliveira, A., Jaguaribe, E.F., 2004. *Conf. Rec. - IEEE Instrum. Meas. Technol. Conf.* 1, 730–733.
- Arlotto, P., Grimaldi, M., Naeck, R., Ginoux, J.M., 2014. *Sensors* 14, 15371–15386. Switzerland.
- Avalur, D.S., 2013. Human Breath Detection Using a Microphone (Netherlands).
- Basu, A., Routray, A., Mukherjee, R., Shit, S., 2016. *Infrared Phys. Technol.* 77, 382–390.
- Bates, A., Ling, M.J., Mann, J., Arvind, D.K., 2010. 2010 Int. Conf. Body Sens. Networks, pp. 144–150. BSN 2010.
- Bifulco, P., Gargiulo, G.D., D'Angelo, G., Liccardo, A., Romano, M., Clemente, F., Cesarelli, M., 2014. In: 20th IMEKO TC4 Symp. Meas. Electr. Quant. Res. Electr. Electron. Meas. Econ. Upturn, Together with 18th TC4 Int. Work. ADC DCA Model. Testing, pp. 786–789. IWADC 2014.
- Bruun, H.H., 1996. *Meas. Sci. Technol.* 7, 1301–1312.
- Cao, Z., Zhu, R., Que, R.Y., 2012. *IEEE Trans. Biomed. Eng.* 59, 3110–3116.
- Chan, A.M., Ferdosi, N., Narasimhan, R., 2013. *Proc. Annu. Int. Conf. IEEE Eng. Med. Biol. Soc. EMBS* 79, 4058–4061.
- Chen, J., Huang, Y., Zhang, N., Zou, H., Liu, R., Tao, C., Fan, X., Wang, Z.L., 2016. *Nat Energy* 1, 16138.
- Chu, M., Nguyen, T., Pandey, V., Zhou, Y., Pham, H.N., Bar-Yoseph, R., Radom-Aizik, S., Jain, R., Cooper, D.M., Khine, M., 2019. *npj Digit. Med.* 2, 8.
- Churi, A., Bhat, A., Mohite, R., Churi, P.P., 2017. 2016 IEEE Int. Conf. Adv. Electron. Commun. Comput. Technol. ICAECC 2, 45–49, 2016.
- Ciaffoni, L., O'Neill, D.P., Couper, J.H., Ritchie, G.A.D., Hancock, G., Robbins, P.A., 2016. *Sci. Adv.* 2, 1–10.



- Dinh, T., Phan, H.P., Nguyen, T.K., Qamar, A., Foissal, A.R.M., Nguyen Viet, T., Tran, C. D., Zhu, Y., Nguyen, N.T., Dao, D.V., 2016. *J. Mater. Chem. C* 4, 10061–10068.
- Dinh, T., Phan, H.P., Nguyen, T.K., Qamar, A., Woodfield, P., Zhu, Y., Nguyen, N.T., Viet Dao, D., 2017. *J. Phys. D Appl. Phys.* 50, 215401.
- Dominelli, P.B., Sheel, A.W., 2012. *Respir. Physiol. Neurobiol.* 180, 147–161.
- Frasca, D., Geraud, L., Charriere, J.M., Debaene, B., Mimoz, O., 2015. *Anaesthesia* 70, 26–31.
- Ghassemi, M.M., Moody, B.E., Lehman, L.H., Song, C., Li, Q., Sun, H., Mark, R.G., Westover, M.B., Clifford, G.D., 2018. In: *Computing in Cardiology Conference*, vol. 45, pp. 1–4.
- Goreke, U., Habibiabad, S., Azgin, K., Beyaz, M.I., 2015. *J. Phys. Conf. Ser.* 660, 12059.
- Hasegawa, Y., Kawaoka, H., Mitsunari, Y., Matsushima, M., Kawabe, T., Shikida, M., 2018. *Microsyst. Technol.* 24, 3455–3465.
- Hung, S.T., Wong, S.C., Fang, W., 2000. *Sensors Actuators, A Phys.* 84, 70–75.
- Jain, C.D., Bhaskar, D.J., Kalra, M., Gandhi, R., Bohra, P., 2015. *The Dental Perception* 1, 7–10.
- Jeong, J.W., Jang, Y.W., Lee, I., Shin, S., Kim, S., 2009. In: *IFMBE Proceedings*.
- Jiang, P., Zhao, S., Zhu, R., 2015. *Sensors* 15, 31738–31750.
- Korppi, M., Don, M., Valent, F., Canciani, M., 2008. *Acta Paediatr. Int. J. Paediatr.* 97, 943–947.
- Lapi, S., Lavorini, F., Borgioli, G., Calzolari, M., Masotti, L., Pistolesi, M., Fontana, G.A., 2014. *Respir. Physiol. Neurobiol.* 191, 60–66.
- Lewis, G.F., Gatto, R.G., Porges, S.W., 2011. *Psychophysiology* 48, 877–887.
- Liu, Z., Zhang, S., Jin, Y.M., Ouyang, H., Zou, Y., Wang, X.X., Xie, L.X., Li, Z., 2017. *Semicond. Sci. Technol.* 32, 64004.
- Mahbub, I., Pullano, S.A., Wang, H., Islam, S.K., Fiorillo, A.S., To, G., Mahfouz, M.R., 2017. *IEEE Sensor. J.* 17, 1858–1864.
- Mailly, F., Giani, A., Bonnot, R., Temple-Boyer, P., Pascal-Delanoy, F., Foucaran, A., Boyer, A., 2001. *Sensors Actuators, A Phys.* 94, 32–38.
- Marin, J.M., Carrizo, S.J., Vicente, E., Agusti, A.G.N., 2005. *Lancet* 365, 1046–1053.
- Massaroni, C., Di Tocco, J., Lo Presti, D., Schena, E., Bressi, F., Bravi, M., Miccinilli, S., Sterzi, S., Longo, U.G., Berton, A., Terracina, P., Carnevale, A., Denaro, V., Formica, D., Saccomandi, P., 2019a. *Appl. MeMeA 2019 - Symp. Proc* 1–6, 2018.
- Massaroni, C., Nicolo, A., Girardi, M., La Camera, A., Schena, E., Sacchetti, M., Silvestri, S., Taffoni, F., 2019b. *IEEE Sensor. J.* 19, 4652–4659.
- Meng, E., Li, P.Y., Tai, Y.C., 2008. *Sensors Actuators, A Phys.* 144, 18–28.
- Meng, K., Zhao, S., Zhou, Y., Wu, Y., Zhang, S., He, Q., Wang, X., Zhou, Z., Fan, W., Tan, X., Yang, J., Chen, J., 2020. *Matter* 2, 896–907.
- Montuschi, P., Mores, N., Trov , A., Mondino, C., Barnes, P.J., 2013. *Respiration* 85, 72–84.
- Myers, C.S., Rabiner, L.R., 1981. *IEEE Trans. Acoust.* 60, 1389–1409.
- Nam, Y., Reyes, B.A., Chon, K.H., 2016. *IEEE J. Biomed. Heal. Informatics* 20, 1493–1501.
- Pereira, C.B., Yu, X., Czaplik, M., Rossaint, R., Blazek, V., Leonhardt, S., 2015. *Biomed. Optic Express* 6, 4378.
- Petitjean, F., Ketterlin, A., Ga arski, P., 2011. *Pattern Recogn.* 44, 678–693.
- Que, R., Zhu, R., 2012. *Sensors* 12, 10920–10929.
- Schena, E., Massaroni, C., Saccomandi, P., Cecchini, S., 2015. *Med. Eng. Phys.* 37, 257–264.
- Schon, S., Theodore, S.J., G ntner, A.T., 2018. *Sensor. Actuator. B Chem.* 273, 1780–1785.
- Senin, P., 2008. *Dynamic Time Warping Algorithm Review* (Honolulu, USA).
- Sepp , V.P., Viik, J., Hyttinen, J., 2010. *IEEE Trans. Biomed. Eng.* 57, 2277–2285.
- Shao, D., Yang, Y., Liu, C., Tsow, F., Yu, H., Tao, N., 2014. *IEEE Trans. Biomed. Eng.* 61, 2760–2767.
- Stehning, C., B rner, P., Nehrke, K., Eggers, H., Stuber, M., 2005. *Magn. Reson. Med.* 54, 476–480.
- Su, Y., Wang, J., Wang, B., Yang, T., Yang, B., Xie, G., Zhou, Y., Zhang, S., Tai, H., Cai, Z., Chen, G., Jiang, Y., Chen, L., Chen, J., 2020. *ACS Nano*. <https://doi.org/10.1021/acsnano.0c01804>.
- Su, Y., Xie, G., Chen, J., Du, H., Zhang, H., Yuan, Z., Ye, Z., Du, X., Tai, H., Jiang, Y., 2016. *RSC Adv.* 6, 97840–97847.
- Vaessen, T.J.A., Overeem, S., Sitskoorn, M.M., 2015. *Sleep Med. Rev.* 19, 51–58.
- Watkins, R.R., Lemonovich, T.L., 2011. *Am. Fam. Physician* 83, 1299–1306.
- Yaggi, H.K., Concato, J., Kernan, W.N., Lichtman, J.H., Brass, L.M., Mohsenin, V., 2005. *N. Engl. J. Med.* 353, 2034–2041.
- Yahya, O., Faezipour, M., 2014. In: *Proc. 2014 Zo. 1 Conf. Am. Soc. Eng. Educ. - "Engineering Educ. Ind. Involve. Interdiscip. Trends," ASEE Zo*, pp. 1–5.
- Yan, C., Gao, Y., Zhao, S., Zhang, S., Zhou, Y., Deng, W., 2020. *Nanomater. Energy* 67, 104235.
- Yoon, J.W., Noh, Y.S., Kwon, Y.S., Kim, W.K., Yoon, H.R., 2014. *J. Electr. Eng. Technol.* 9, 334–343.
- Zhang, N., Huang, F., Zhao, S., Nie, Y., Fan, X., Zhang, N., Huang, F., Zhao, S., Lv, X., Zhou, Y., Xiang, S., 2020. *Matter* 1–10.
- Zhao, S., Zhu, R., 2017. *Adv. Mater.* 29.
- Zhou, Z., Padgett, S., Cai, Z., Conta, G., Wu, Y., He, Q., Zhang, S., Sun, C., Liu, J., Fan, E., Meng, K., Lin, Z., Uy, C., Yang, J., Chen, J., 2020. *Biosens. Bioelectron.* 155, 112064.